$L1_0$ Fe-Pd Synthetic Antiferromagnet through an fcc Ru Spacer Utilized for Perpendicular Magnetic Tunnel Junctions

De-Lin Zhang,[1] Congli Sun,[3] Yang Lv,[1] Karl B. Schliep,[2] Zhengyang Zhao,[1] Jun-Yang Chen,[1] Paul M. Voyles,[3] and Jian-Ping Wang[1,*]

[1]*Department of Electrical and Computer Engineering, University of Minnesota, Minneapolis, Minnesota 55455, USA*
[2]*Department of Chemical Engineering and Materials Science, University of Minnesota, Minneapolis, Minnesota 55455, USA*
[3]*Department of Materials Science and Engineering, University of Wisconsin-Madison, Madison, Wisconsin 53706, USA*

Magnetic materials that possess large bulk perpendicular magnetic anisotropy (PMA) are essential for the development of magnetic tunnel junctions (MTJs) used in future spintronic memory and logic devices. The addition of an antiferromagnetic layer to these MTJs was recently predicted to facilitate ultrafast magnetization switching. Here, we report a demonstration of a bulk perpendicular synthetic antiferromagnetic (PSAFM) structure comprised of a (001) textured Fe-Pd/Ru/Fe-Pd trilayer with a face-centered-cubic (fcc) phase Ru spacer. The $L1_0$ Fe-Pd PSAFM structure shows a large bulk PMA ($K_u \sim 10.2$ Merg/cm^3) and strong antiferromagnetic coupling ($-J_{\mathrm{IEC}} \sim 2.60$ erg/cm^2). Full perpendicular magnetic tunnel junctions (PMTJs) with a $L1_0$ Fe-Pd PSAFM layer are then fabricated. Tunneling magnetoresistance ratios of up to approximately 25% (approximately 60%) are observed at room temperature (5 K) after postannealing at 350 °C. Exhibiting high thermal stabilities and large K_u, the bulk PMTJs with an $L1_0$ Fe-Pd PSAFM layer could pave a way for next-generation ultrahigh-density and ultralow-energy spintronic applications.

I. INTRODUCTION

Magnetic materials that exhibit perpendicular magnetic anisotropy (PMA) are promising candidates for the development of ultrahigh-density and ultralow-energy spintronic memory and logic devices due to their high thermal stability and scalability [1–4]. Recently, interfacial PMA materials have made considerable progress in the application of spin-transfer-torque magnetic random-access memory (STT MRAM) [5–8]. However, because of their relatively low PMA value ($K_u \sim 2$–5 Merg/cm^3) and relatively large damping constant ($\alpha \sim 0.015$–0.027) [5,9,10], they may not fully satisfy the scaling demands needed for next-generation spintronic memory and logic devices. When scaling spintronic devices to commercially sustainable sizes, like 10-nm nodes, large K_u and low α values are required to realize longer retention times and ultralow switching current densities. The manganese- (Mn) based Heusler alloys [11–15] and $L1_0$ Fe-Pd are promising candidates for satisfying these requirements. Compared with the Mn-based Heusler alloys, the $L1_0$ Fe-Pd bulk PMA material possesses very attractive properties, such as a large K_u (13–14 Merg/cm^3) [16,17], a low α (0.002)

[18,19], and a low processing temperature (200 °C) [20], which are summarized in Table I. Furthermore, the switching current density (J_c) for spintronic memory devices, such as STT MRAM, is a critical parameter defined by the equation $J_c = 2\alpha e t_F M_s (H_{\mathrm{appl}} + H_k)/\hbar\eta$ [21], where J_c mainly relates to the α, the saturation magnetization (M_S), and the perpendicular anisotropy field (H_k). From this equation, it is clear that a small M_S and low α value should be pursued to reduce the J_c value. For $L1_0$ Fe-Pd thin films, the low $\alpha \sim 0.002$ is demonstrated experimentally; however, the M_S of approximately 1100 emu/cm^3 is relatively high. A promising solution to lower its M_S is to develop a synthetic antiferromagnetic (SAFM) structure [22,23] in which two ferromagnetic layers are coupled antiferromagnetically through a spacer so that the magnetization can be reduced. The SAFM structure is also being pursued because it was theoretically predicted to significantly increase the switching speed and reduce the J_c value in the MTJ devices [24,25]. Additionally, the velocity of domain-wall motion in the SAFM layers was found to be largely enhanced [26,27]. Current reports on the perpendicular SAFM (PSAFM) structures have been increasingly focused on the $[\mathrm{Co/Pd}]_n$ [28,29] and $[\mathrm{Co/Pt}]_n$ [30,31] multilayer systems. However, the disadvantages of these PSAFM systems are that they have (111) texture, making it difficult to

*To whom correspondence should be addressed. jpwang@umn.edu

TABLE I. Comparison of magnetic properties and TMR ratio of the PMA Mn-based Heusler films and the $L1_0$-phase PMA Fe-Pd film.

	Mn-based Heusler film	$L1_0$-phase Fe-Pd film
Spin polarization	58% [11]	$\cdots$
Damping constant	0.015–0.008 [12]; 0.03 [13]	0.007 [17]; 0.002–0.004 [19]
Magnetization	150–500 emu/cm^3	<500 emu/cc (PSAFM)
Magnetic anisotropy	<10 Merg/cm^3 ($t < 20$ nm)	11 Merg/cc (3.5 nm) [17]
Thickness (t) in MTJ	>20 nm	3–7 nm
Lattice constant	$a = 3.92$ Å, $c = 7.10$ Å	$a = 3.90$ Å, $c = 3.72$ Å
RT TMR ratio	24% (300 °C) [14]	27% (325 °C with in-plane reference layer) [15]; 25% (350 °C) (this work)

epitaxially grow on the MgO (001) tunnel barrier, and they have larger α and limited K_u values compared with the $L1_0$ Fe-Pd PSAFM structure investigated here.

In this work, we demonstrate a $L1_0$ Fe-Pd PSAFM structure and a $L1_0$ Fe-Pd synthetic antiferromagnetic perpendicular magnetic tunnel junction (named $L1_0$ Fe-Pd SAFM PMTJ). The $L1_0$ Fe-Pd PSAFM structure grown here with a (001) texture possesses a high $K_u \sim 10.2$ Merg/cm^3 and low net remanent magnetization (approximately 500 emu/cm^3). One of the most important discoveries here is the epitaxial growth of a ruthenium (Ru) spacer with a face-centered-cubic (fcc) phase on the $L1_0$ Fe-Pd thin film, which results in a large interlayer exchange coupling (IEC) $-J_{IEC} \sim 2.60$ erg/cm^2. This value is about 1 order of magnitude larger than that of the $[Co/Pd]_n$ or $[Co/Pt]_n$ PSAFM structures. Moreover, a tunneling magnetoresistance (TMR) ratio of approximately 25.0% tested at room temperature (RT) is obtained in the $L1_0$ Fe-Pd SAFM PMTJ devices with the $L1_0$ Fe-Pd PSAFM layer after postannealing at 350 °C. Furthermore, a TMR ratio of approximately 13% is retained when the postannealing temperature is increased to 400 °C, implying that this kind of Fe-Pd SAFM PMTJ can be integrated into the semiconductor process.

II. EXPERIMENT

All samples are deposited on (001) single-crystal MgO substrates using an ultrahigh-vacuum magnetron sputtering systems with a base pressure less than 5.0×10^{-8} Torr. During the deposition of the Cr(15 nm)/Pt(5 nm) seed layer, Fe-Pd, and Ru layers, the substrate temperature is kept at 350 °C. The pressure of the Ar working gas is set at 4.5 mTorr for the Fe-Pd layer and 2.0 mTorr for the other layers. The Fe-Pd thin films are prepared by cosputtering with the Fe and Pd targets. The composition is determined to be Fe$_{53.2}$Pd$_{46.8}$ by Rutherford backscattering spectrometry. After the Fe-Pd layer deposition, the films are cooled to RT. Subsequently, a 5-nm-thick Ta capping layer is grown on the single-layer Fe-Pd film and Fe-Pd PSAFM structure to facilitate the investigation of their magnetic properties. The Ta(0.8)/Co$_{20}$Fe$_{60}$B$_{20}$(1.3)/MgO(2)/Co$_{20}$Fe$_{60}$B$_{20}$(1.3)/Ta(0.7)/[Pd(0.7)/Co(0.3)]$_4$/Ta(5) stack

(the unit in nanometers) is grown on the Fe-Pd PSAFM structure to fabricate the full Fe-Pd SAFM PMTJ stack. The structural properties of the Fe-Pd PSAFM structure and the Fe-Pd SAFM PMTJ stack are characterized by out-of-plane (θ–2θ scan) x-ray diffraction (XRD) with Cu $K\alpha$ radiation ($\lambda = 0.15418$ nm) using a Bruker D8 Discover system and scanning transmission electron microscopy (STEM), whereas the magnetic properties are determined using a physical property measurement system (PPMS). Cross-sectional STEM samples of the $L1_0$ Fe-Pd PSAFM structure and the $L1_0$ Fe-Pd SAFM PMTJ stack are prepared by an *in situ* lift-out method using a Zeiss Auriga focused-ion-beam system. STEM imaging is performed on a FEI Titan with a CEOS probe aberration corrector operated at 200 kV with a probe convergence angle of 24.5 mrad, spatial resolution of 0.08 nm, and probe current of approximately 20 pA.

The $L1_0$ Fe-Pd SAFM PMTJ stacks are patterned into micron-sized pillars with diameters ranging from 4 to 20 μm by conventional photolithography and an Ar ion milling process. Electrical contacts are formed from Ti(10 nm)/Au(120 nm). The patterned MTJ devices are annealed from 300 to 400 °C by a rapid-thermal-annealing (RTA) process. The magnetotransport properties of the patterned MTJs are measured at different temperatures between 5 and 300 K using a dc four-probe method used with a Quantum Design PPMS with a Keithley 6221 current source and 2182 voltmeter. During the measurement, a magnetic field is applied along the out-of-plane (perpendicular) direction, and the positive current is defined as the electron flow from the top reference layer to the bottom free layer of the $L1_0$ Fe-Pd SAFM PMTJ devices.

III. RESULTS AND DISCUSSION

A. Magnetic properties of the $L1_0$ Fe-Pd PSAFM structure

First, we prepare an 8-nm-thick Fe-Pd single-layer thin film on the (001) single-crystal MgO substrate to characterize the crystalline structure and PMA properties. The Cr(15 nm)/Pt(4 nm) buffer layer with *in situ* substrate

temperature of 350 °C is used to induce the (001) texture. The M_S is determined to be approximately 1050 emu/cm^3 from the magnetic hysteresis (M-H) loop, and K_u is evaluated to be 11.5 Merg/cm^3 following the equation $K_u = (M_S H_K/2) + 2\pi M_S^2$ [17]. Here, H_K and M_S are the saturation magnetic field and the saturation magnetization, respectively. These values are close to the values of the $L1_0$ Fe-Pd bulk material (approximately 1100 emu/cm^3 and 18 Merg/cm^3) [16] (see Supplemental Material Fig. 1 in Ref. [32]). After that, the Fe-Pd PSAFM structures with a stack of Fe-Pd(3 nm)/Ru(t_{Ru} nm)/Fe-Pd(3 nm) are grown using the same process as the Fe-Pd single-layer thin film. The schematic of the Fe-Pd SAFM structure is shown in the inset of Fig. 1(a), where two Fe-Pd PMA layers are coupled antiferromagnetically via a thin Ru spacer. The thickness of the Ru spacer (t_{Ru}) is varied from 0.9 to 1.4 nm to track the IEC between two Fe-Pd PMA layers. The observed largest IEC occurs when the thickness of the Ru spacer is around 1.1 nm. Its M-H loops are plotted in Fig. 1(a). We find that the $L1_0$ Fe-Pd PSAFM structure presents good PMA with a square-shaped minor M-H loop and a net remanent magnetization of approximately 500 emu/cm^3. The M_S of the $L1_0$ Fe-Pd PSAFM structure calculated from the M-H loops is approximately 960 emu/cm^3, which is a little lower than that of the single-layer Fe-Pd thin film. One probable reason is the formation of the Fe-PdRu$_x$ alloy at the Ru/Fe-Pd interface due to the Ru diffusion [33]. Meanwhile, H_K is determined to be approximately 8.9 kOe from the in-plane M-H loop. K_u of the Fe-Pd PSAFM structure

is then evaluated to be approximately 10.2 Merg/cm^3 following the equation used before, which is several times larger than that of interfacial PMA materials (e.g., a Ta/Co-Fe-B/MgO structure).

Normally, the shape of the out-of-plane M-H loop of the PSFAM systems depends on the competition between the PMA and the antiferromagnetic coupling, so one can determine the type of antiferromagnetic coupling exhibited from the M-H loop of the PSFAM sample [34]. For the Fe-Pd PSAFM structure as shown in Fig. 1(a), we can clearly observe the spin-flip switching between two Fe-Pd layers at the high external magnetic field. Meanwhile, the spin-flip switching appears at the low external magnetic field, implying that two Fe-Pd layers form the antiferromagnetic alignment. This phenomenon also indicates that the strength of antiferromagnetic coupling between the two Fe-Pd layers is larger than that of the PMA of the Fe-Pd SAFM structure. Following the equation $-4J_{IEC} = H_{ex} M_S t_{FM} + 2K_{u,eff} t_{FM}$ (in this case, $K_u < -J_{IEC}/t$) [34], J_{IEC} of the Fe-Pd PSAFM structure is calculated to be approximately -2.60 erg/cm^2, where $K_{u,eff}$ is the magnetic anisotropy, H_{ex} is the exchange field (approximately 9.2 kOe for the Fe-Pd SAFM structure), and t_{FM} is the thickness of the Fe-Pd PMA layer. This value is about 1 order of magnitude larger than that of the [Co/Pd]$_n$ PSAFM system with the same postannealing temperature [29]. In addition, previous reports show that the moderate antiferromagnetic exchange coupling performance can be observed at the second peak of oscillation with $t_{Ru} \sim$ 0.9 nm [35]. The difference in the optimal Ru thickness ($t_{Ru} \sim 1.1$ nm) in this work is attributed to the relatively large roughness (approximately 0.30 nm) from the Cr/Pt seed layer and the high deposition temperature used. This result is similar to that of the postannealed [Co/Pd]$_n$ PSAFM structure with the strongest J_{IEC} when the t_{Ru} is approximately 1.3 nm thick [29].

B. Structural properties of the $L1_0$ Fe-Pd PSAFM structure

The crystalline structure of the $L1_0$ Fe-Pd PSAFM structure with an 1.1-nm-thick Ru spacer is characterized by XRD. The results are shown in Fig. 1(b). The (001) and (002) peaks from the $L1_0$ Fe-Pd layers and (002) peak from Cr and Pt seed layers are clearly visible, suggesting a well-formed superlattice structure. Because the $t_{Ru} \sim 1.1$ nm is thin, it is difficult to observe the Ru peak by the XRD measurement. To identify the crystalline structure of the Ru spacer and the epitaxial relationship of the Ru and Fe-Pd layers, aberration-corrected STEM is performed to characterize the atomic structures. Figure 2(a) shows the high-angle annular-dark-field (HAADF) STEM images of the $L1_0$ Fe-Pd PSAFM structure (the HAADF signal scales with Z^a; here, Z is the atomic number of the element, and the "a" is the coefficient, so the image is dominated by high-Z atomic sites). As shown in Fig. 2(a), the (001)
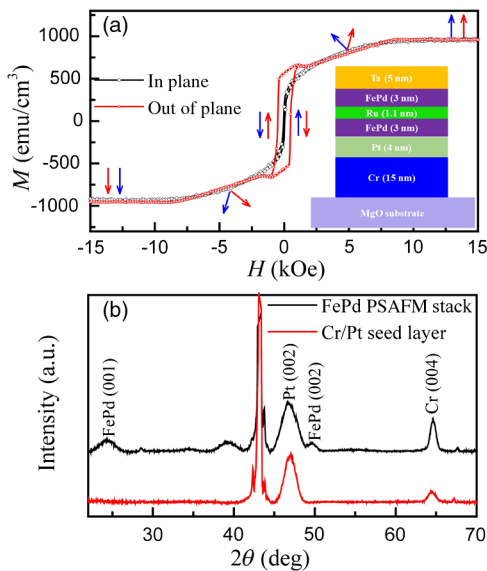

FIG. 1. (a) The M-H loops of the Fe-Pd(3 nm)/Ru(1.1 nm)/Fe-Pd(3 nm) PSAFM structure measured at room temperature. The inset of (a) shows the schematic diagram of the $L1_0$ Fe-Pd PSAFM structure. The Cr and Pt buffer layers are used to induce the (001) texture, and the thin Ru layer is used as a spacer. (b) XRD pattern with out-of-plane θ–2θ scans for the $L1_0$ Fe-Pd PSAFM structure; the Cr/Pt buffer layer is used as a reference.
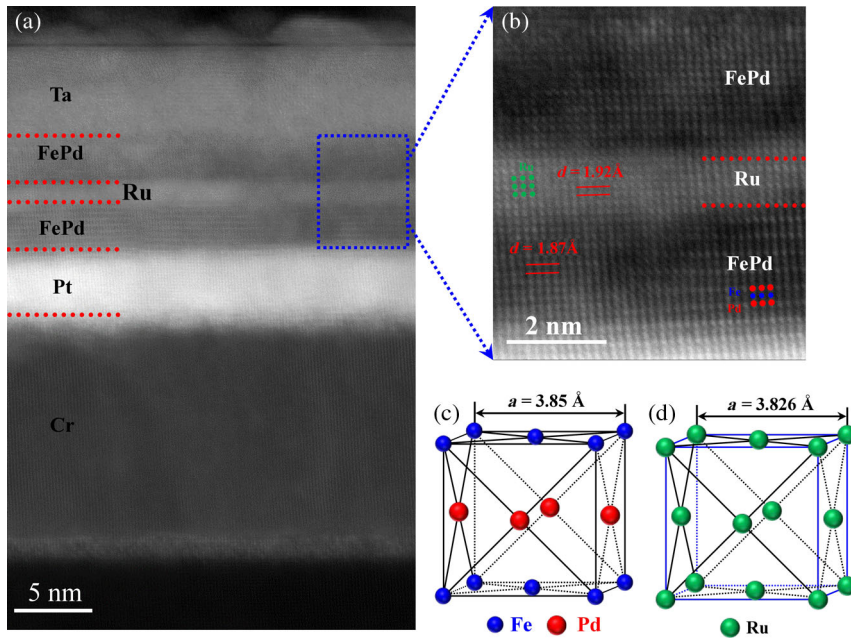
FIG. 2. (a) HAADF STEM images of the $L1_0$ Fe-Pd PSAFM structure; the clearly epitaxial layered structure is observed. (b) A magnified STEM image of the Fe-Pd/Ru/Fe-Pd trilayer, which shows the smooth interface between the Fe-Pd and Ru layers. Meanwhile, the lattice spacing of the Fe-Pd and Ru layers is calculated from TEM; labeling in TEM image. (c) The crystalline structure of the Fe-Pd material with the tetragonal AuCu-type phase. The blue (small) ball denotes the Fe atom, and the red (big) ball represents the Pd atom. (d) The crystalline structure of the Ru material with fcc phase. The fcc phase Ru thin films are not experimentally realized; they are just theoretically predicted by first-principles calculation. Its theoretical lattice constant is $a = b = c = 0.3826$ nm.

epitaxial relationship is observed throughout the film, starting with the MgO (001) surface and continuing through each layer of the stack along the vertical direction. Meanwhile, we find that the Cr layer is oxidized in the Cr/MgO interface, and the Pt/Cr interface is rough but other layers form the sharp interface. The crystalline structure of the Ru spacer and the Fe-Pd layer is determined by the magnified HAADF STEM image as shown in Fig. 2(b). From the STEM image, one can see that the bottom Fe-Pd layer matches the (001) texture of the Pt/Cr seed layer with the epitaxial relationship Cr[110](001)∥Pt[100](001)∥Fe-Pd[100](001). The average lattice spacing of two atomic planes along the (001) direction of the Fe-Pd layer measured from the STEM image is 0.187 nm close to the lattice constant of the tetragonal AuCu-type Fe-Pd structure shown in Fig. 2(c).

Normally, the Ru spacer forms the hexagonal-close-packed (hcp) phase like in the Co/Ru [35] and $[Co/Pd]_n$/Ru SAFM systems [29], generating the periodic oscillations of antiferromagnetic coupling due to the Ruderman-Kittel-Kasuya-Yosida interaction [35]. In our experiment, the Ru spacer interestingly also follows the (001)-oriented growth of the bottom Fe-Pd layer. The average in-plane lattice spacing is estimated to be 0.192 nm from the STEM image, which matches very well with the lattice spacing of the fcc phase Ru structure predicted by a first-principles calculation [36], as shown in Fig. 2(d). The highly textured growth of the Ru spacer on the Fe-Pd layer is due to a very small lattice mismatch (0.62%) between the $L1_0$ Fe-Pd and the fcc phase Ru layers. This fcc phase Ru layer also induces the (001) texture of the top Fe-Pd layer with the $L1_0$ phase. The epitaxial relationship of the Fe-Pd/Ru/Fe-Pd trilayer is also determined to be Fe-Pd[100](001)∥Ru[100](001)∥Fe-Pd[100](001). In addition, the STEM image with a 90° in-plane rotation of the

TEM sample is used to confirm the texture of the Fe-Pd/Ru/Fe-Pd stack. The same epitaxial relationship as shown in Fig. 2(a) is observed in the Fe-Pd/Ru/Fe-Pd trilayer (Fig. 2 in Ref. [32]). The results of the $L1_0$ Fe-Pd PSAFM structure indicate that not only does the Ru spacer on the (001) texture Fe-Pd layer present the fcc phase, but also the fcc phase Ru spacer can result in a larger antiferromagnetic coupling.

C. Magnetic properties of the $L1_0$ Fe-Pd SAFM PMTJ stack

Based on the developed $L1_0$ Fe-Pd PSAFM structure, which has a relatively smooth surface with root-mean-square surface roughness of approximately 0.30 nm (Fig. 3 in Ref. [32]), we design and fabricate a full $L1_0$ Fe-Pd SAFM PMTJ stack as shown in Fig. 3(a). Using Ta or other metal layer to couple a hard magnetic layer with Co-Fe-B has been proposed and established as a standard for STT RAM cells [37]. In this $L1_0$ Fe-Pd SAFM PMTJ stack, a composite layer with a stack of Fe-Pd/Ru/Fe-Pd/Ta/Co-Fe-B is designed as the bottom free layer, where the Fe-Pd PSAFM trilayer couples with the Co-Fe-B layer through a thin Ta layer. Meanwhile, a composite layer with a stack of Co-Fe-B/Ta/$[Co/Pd]_n$ is designed as the top reference layer. A 1.3-nm-thick $Co_{20}Fe_{60}B_{20}$ (Co-Fe-B) layer is introduced adjacent to the MgO barrier to enhance the TMR ratio. An ultrathin Ta layer (approximately 0.7 nm) is inserted between the Co-Fe-B and Fe-Pd ($[Co/Pd]_n$) layers to mitigate Pd diffusion that occurs during the high-temperature annealing process [38].

The quality of the MgO tunnel barrier plays a significant role in obtaining a large TMR ratio in the MgO-barrier MTJ devices. The annular-bright-field (ABF) STEM is employed to determine the atomic structure of the MgO barrier in the $L1_0$ Fe-Pd SAFM PMTJ stack postannealed at
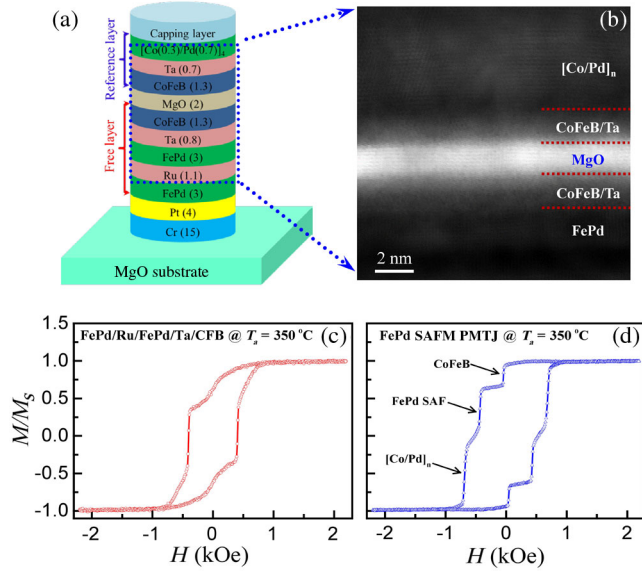
FIG. 3. (a) A schematic illustration of the $L1_0$ Fe-Pd SAFM PMTJ stack in which the $L1_0$ Fe-Pd PSAFM layer couples with the Co-Fe-B layer through a thin Ta layer to form the bottom free layer. The $[Co/Pd]_n$ and Co-Fe-B layers form the top reference layer by a thin Ta layer. The thin Ta layer plays a very important role as the coupling spacer and diffusion barrier, which can be used to block the Pd diffusion when the MTJ devices are annealed at high temperature. (b) The ABF STEM image of the Co-Fe-B/MgO/Co-Fe-B region of the $L1_0$ Fe-Pd SAFM PMTJ stack, which is used to determine the quality of the MgO tunneling barrier. (c),(d) The room-temperature out-of-plane M-H loops of the Fe-Pd free layer with a stack of Fe-Pd/Ru/Fe-Pd/Ta/Co-Fe-B and the $L1_0$ Fe-Pd SAFM PMTJ stack. These stacks are postannealed at 350 °C by the RTA process.

350 °C. From the ABF STEM image shown in Fig. 3(b), we can see that the MgO tunnel barrier layer crystallizes into a (001) textured structure, and a sharp MgO/Co-Fe-B interface can be observed. The magnetic properties of the Fe-Pd PSAFM free layer and the $L1_0$ Fe-Pd SAFM PMTJ stack are characterized individually after the samples are post-annealed at 350 °C. Their out-of-plane M-H loops are shown in Figs. 3(c) and 3(d), respectively. From the M-H loop shown in Fig. 3(c), it is evident that the Fe-Pd PSAFM free layer possesses a PMA with an antiferromagnetic coupling between the Fe-Pd PSAFM and Co-Fe-B layers. H_C of the Fe-Pd PSAFM free layer is found to be approximately 390 Oe. The saturation magnetic field H_s of the Fe-Pd free layer is slightly enhanced compared with the $L1_0$ Fe-Pd PSAFM stack. This H_s enhancement is similar to what is observed in the Co-Fe-B/Ta/Co-Fe-B PSAFM stack [39].

Before integrating the $[Co/Pd]_n$ reference layer into the $L1_0$ Fe-Pd SAFM PMTJ stack, its magnetic property and thermal stability are studied. After postannealing using the same experimental condition as the Fe-Pd free layer, the $[Co/Pd]_n$ reference layer shows a square-shaped M-H loop

with H_C of approximately 1400 Oe, and a high-quality (111) texture is also observed (Fig. 4 in Ref. [32]). Figure 3(d) depicts the magnetic properties of the $L1_0$ Fe-Pd SAFM PMTJ stack with postannealing temperature of 350 °C. Three-step switching of the magnetization is observed. The first and second switching fields $H_{swf1} \sim 39$ Oe and $H_{swf2} \sim 390$ Oe correspond to the Co-Fe-B and $L1_0$ Fe-Pd PSAFM layers, respectively. The third switching is from the $[Co/Pd]_n$ reference layer with $H_{swf} \sim 700$ Oe, which is smaller than that of the $[Co/Pd]_n$ reference layer on Si/SiO$_2$ substrate. The main reason is that the (001) texture of the bottom $L1_0$ Fe-Pd PSAFM free layer results in the lattice mismatch and affects the (111) texture of the $[Co/Pd]_n$ layer. The M-H loops of the Fe-Pd free layer and the $L1_0$ Fe-Pd SAFM PMTJ stack postannealed at 400 °C show the same trend as the sample postannealed at 350 °C (Fig. 5 in Ref. [32]).

D. Magnetotransport properties of the $L1_0$ Fe-Pd SAFM PMTJ devices

To study the magnetotransport property and thermal stability of the proposed structures, the $L1_0$ Fe-Pd SAFM PMTJ stack illustrated in Fig. 3(a) is patterned into micron-size pillars with diameters ranging from 4 to 20 μm using a standard lithography patterning process. After patterning, these devices are postannealed from 300 to 400 °C by a RTA process. The TMR versus external magnetic field (TMR-H) loops of the $L1_0$ Fe-Pd SAFM PMTJ devices presented in the inset of Fig. 4(e) are tested at RT by a standard four-probe resistance measurement technique. The TMR-H loops of the 12-μm-diameter $L1_0$ Fe-Pd SAFM PMTJ devices are plotted in Figs. 4(a)–4(d). From these RT TMR-H loops, we can observe a plateau in the high-resistance state and a sharp magnetization switching between the parallel state and the antiparallel state while sweeping the perpendicular external magnetic field. This result suggests that the Fe-Pd free layer and the $[Co/Pd]_n$ reference layer possess a good PMA even after postanneal-ing up to 400 °C. As depicted in Fig. 4(e), with the increase of the postannealing temperature from 300 to 350 °C, the TMR ratio slightly increases from approximately 24% to approximately 25%. Then, the TMR ratio decreases to approximately 13% with the increasing of the annealing temperature up to 400 °C, which indicates that the Fe-Pd SAFM PMTJs devices have a good thermal stability. The decrease of the TMR ratio for the $L1_0$ Fe-Pd SAFM PMTJ devices may be due to three reasons: one reason is the interlayer diffusion of the Ta or Pd atoms into the Co-Fe-B layer to form the Co-Fe-BTa$_x$ or Co-Fe-BPd$_x$ thin layers. Another reason is that the Co-Fe-B layer is oxidized at the Co-Fe-B/MgO interface to form the dead layer. The third reason is that boron atoms diffuse into the MgO tunnel barrier after the high-temperature thermal treatment. These reasons lead to low spin polarization of the Co-Fe-B layer, create surface magnetization instability, and produce
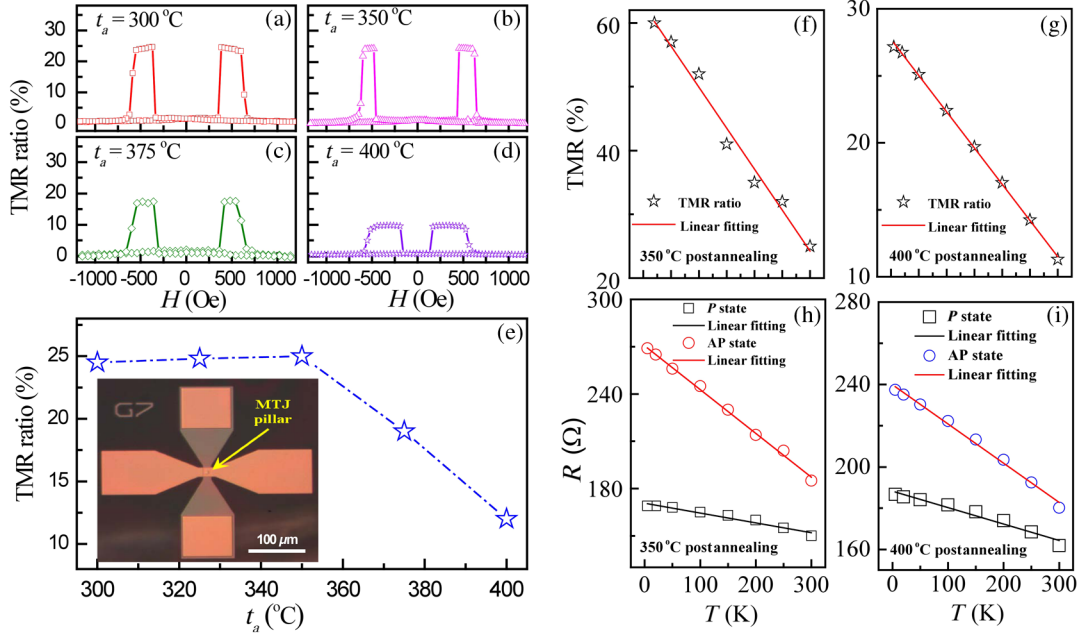
FIG. 4. The tunneling magnetoresistance versus external magnetic field (TMR-H) loops of the $L1_0$ Fe-Pd SAFM PMTJ devices postannealed by RTA at (a) 300 °C, (b) 350 °C, (c) 375 °C, and (d) 400 °C. The testing is carried out at room temperature. The external magnetic field is swapped from -1500 to $+1500$ Oe along the perpendicular plane of the devices. (e) The TMR ratio as a function of the postannealing temperatures of the $L1_0$ Fe-Pd SAFM PMTJ devices. The inset is the optical microscopy image of the real $L1_0$ Fe-Pd SAFM PMTJ device. (f),(g) TMR ratio as a function of the annealing temperatures for the $L1_0$ Fe-Pd SAFM PMTJ devices annealed at 350 and 400 °C, respectively. (h),(i) The temperature dependence of the resistance of the parallel state (open squares) and the antiparallel state (open circles) in the $L1_0$ Fe-Pd SAFM PMTJ devices annealed at 350 °C and 400 °C, respectively.

elemental impurities in the MgO tunnel barrier. These factors can strongly affect the magnetotransport properties of the PMTJs [40,41]. For the MgO-barrier MTJs, the giant TMR ratio is attributed to the spin-dependent coherent tunneling through the Δ_1 Bloch state in the high-quality (001) epitaxial MgO tunnel barrier [42].

In order to understand the tunneling behavior (coherent or incoherent tunneling) of the $L1_0$ Fe-Pd SAFM PMTJ devices, we investigate the TMR ratio as a function of the temperatures. The TMR-H loops are tested from 5 to 300 K for the 12-μm-diameter $L1_0$ Fe-Pd SAFM PMTJ devices postannealed at 350 °C and 400 °C, respectively, by a Quantum Design PPMS. The results are plotted in Figs. 4(f) and 4(g). We can clearly see that the TMR ratio gradually increases from approximately 25% up to approximately 60% for the junctions annealed at 350 °C and from approximately 13% up to approximately 27% for the junctions annealed at 400 °C while the testing temperature goes down from 300 to 5 K. The increase of the TMR ratio mainly originates from the increase of the R_{AP} value, which dominates the TMR ratio. However, the R_P value presents weak temperature dependence for both PMTJs, as shown in Figs. 4(h) and 4(i). Coherent tunneling behavior is illustrated by a dramatic increase in R_{AP}, while R_P remains constant when the testing temperature is decreased [41]. From Figs. 4(h) and 4(i), we can deduce that the $L1_0$ Fe-Pd SAFM PMTJ devices annealed at 350 and 400 °C show

nonperfect coherent tunnel behavior. This explains why the $L1_0$ Fe-Pd SAFM PMTJ devices show the relatively low TMR ratio at RT, which may be due to the elemental diffusion or dead layer mentioned before.

To further understand these devices, the normalized TMR ratio as a function of bias voltage (V) is investigated. The V_{half} defined as the bias voltage at which the TMR ratio drops to one-half of the zero-bias value is a crucial factor for the device application in ultrahigh-density MRAM. The V_{half} of the $L1_0$ Fe-Pd SAFM PMTJ devices annealed at 350 °C (400 °C) is determined to be approximately 380 mV (approximately 370 mV) and approximately 400 mV (approximately 470 mV) for positive- and negative-bias voltage, respectively. This is just a little lower than that of Co_2FeAl (theoretical 100% spin polarization of the half-metallic Heusler alloy) in-plane MTJs with the MgO tunneling barrier (500 mV for positive-bias and 600 mV for negative-bias directions) (Fig. 6 in Ref. [32]).

IV. CONCLUSIONS

We realize a bulk perpendicular SAFM structure and the integration of a PMTJ stack using the $L1_0$-PMA Fe-Pd thin films. The (001) epitaxial $L1_0$ Fe-Pd PSAFM structure shows large antiferromagnetic coupling ($-J_{IEC} \sim 2.60$ erg/cm^2) with a high $K_u \sim 10.2$ Merg/cm^3 and a low net remanent magnetization (approximately

500 emu/cm^3). High RT TMR ratios up to approximately 25% (approximately 13%) are achieved for the $L1_0$ Fe-Pd SAFM PMTJ devices postannealed at 350 °C (400 °C) using the Fe-Pd free layer, which suggests that the $L1_0$ Fe-Pd SAFM PMTJs can adhere to standard back-end-of-line processes. Furthermore, the $L1_0$ Fe-Pd PSAFM structure can be also used to study the domain-wall motion, spin-orbit torques [43], Skyrmion [44], and antiferromagnetic spintronics [45]. These combined results provide significant potential in scaling PMTJs below 10 nm for applications on spintronic memory and logic devices. Further optimization of the deposition process and patterning process is under way to improve its TMR ratio.

ACKNOWLEDGMENTS

---

[1] H. Meng and J. P. Wang, Spin transfer in nanomagnetic devices with perpendicular anisotropy, Appl. Phys. Lett. **88,** 172506 (2006).

[2] S. Mangin, D. Ravelosona, J. A. Katine, M. J. Carey, B. D. Terris, and E. E. Fullerton, Current-induced magnetization reversal in nanopillars with perpendicular anisotropy, Nat. Mater. **5,** 210 (2006).

[3] Z. Li, S. Zhang, Z. Diao, Y. Ding, X. Tang, D. M. Apalkov, Z. Yang, K. Kawabata, and Y. Huai, Perpendicular Spin Torques in Magnetic Tunnel Junctions, Phys. Rev. Lett. **100,** 246602 (2008).

[4] A. D. Kent and D. C. Worledge, A new spin on magnetic memories, Nat. Nanotechnol. **10,** 187 (2015).

[5] S. Ikeda, K. Miura, H. Yamamoto, K. Mizunuma, H. D. Gan, M. Endo, S. Kanai, J. Hayakawa, F. Matsukura, and H. Ohno, A perpendicular-anisotropy CoFeB-MgO magnetic tunnel junction, Nat. Mater. **9,** 721 (2010).

[6] P. K. Amiri, Z. M. Zeng, J. Langer, H. Zhao, G. Rowlands, Y.-J. Chen, I. N. Krivorotov, J.-P. Wang, H. W. Jiang, J. A. Katine, Y. Huai, K. Galatsis, and K. L. Wang, Switching current reduction using perpendicular anisotropy in CoFeB-MgO magnetic tunnel junctions, Appl. Phys. Lett. **98,** 112507 (2011).

[7] H. Sato, E. C. I. Enobio, M. Yamanouchi, S. Ikeda, S. Fukami, S. Kanai, F. Matsukura, and H. Ohno, Properties of magnetic tunnel junctions with a MgO/CoFeB/Ta/CoFeB/MgO recording structure down to junction diameter of 11 nm, Appl. Phys. Lett. **105,** 062403 (2014).

[8] W.-G. Wang, M. Li, S. Hageman, and C. L. Chien, Electric-field-assisted switching in magnetic tunnel junctions, Nat. Mater. **11,** 64 (2012).

[9] H. Sato, M. Yamanouchi, K. Miura, S. Ikeda, H. D. Gan, K. Mizunuma, R. Koizumi, F. Matsukura, and H. Ohno, Junction size effect on switching current and thermal stability in CoFeB/MgO perpendicular magnetic tunnel junctions, Appl. Phys. Lett. **99,** 042501 (2011).

[10] S. Iihama, S. Mizukami, H. Naganuma, M. Oogane, Y. Ando, and T. Miyazaki, Gilbert damping constants of Ta/CoFeB/MgO(Ta) thin films measured by optical detection of precessional magnetization dynamics, Phys. Rev. B **89,** 174416 (2014).

[11] H. Kurt, K. Rode, M. Venkatesan, P. Stamenov, and J. M. D. Coey, High spin polarization in epitaxial films of ferrimagnetic Mn_3Ga, Phys. Rev. B **83,** 020405(R) (2011).

[12] S. Mizukami, F. Wu, A. Sakuma, J. Walowski, D. Watanabe, T. Kubota, X. Zhang, H. Naganuma, M. Oogane, Y. Ando, and T. Miyazaki, Long-Lived Ultrafast Spin Precession in Manganese Alloys Films with a Large Perpendicular Magnetic Anisotropy, Phys. Rev. Lett. **106,** 117201 (2011).

[13] S. Mizukami, A. Sugihara, S. Iihama, Y. Sasaki, K. Z. Suzuki, and T. Miyazaki, Laser-induced THz magnetization precession for a tetragonal Heusler-like nearly compensated ferromagnet, Appl. Phys. Lett. **108,** 012404 (2016).

[14] T. Kubota, Q. L. Ma, S. Mizukami, X. M. Zhang, H. Naganuma, M. Oogane, Y. Ando, and T. Miyazaki, Magnetic tunnel junctions of perpendicularly magnetized $L1_0$-MnGa/Fe/MgO/CoFe structures: Fe-layer-thickness dependences of magnetoresistance effect and tunnelling conductance spectra, J. Phys. D **46,** 155001 (2013).

[15] H. Naganuma, G. Kim, Y. Kawada, N. Inami, K. Hatakeyama, S. Iihama, K. M. N. Islam, M. Oogane, S. Mizukami, and Y. Ando, Electrical detection of millimeter-waves by magnetic tunnel junctions using perpendicular magnetized $L1_0$-FePd free layer, Nano Lett. **15,** 623 (2015).

[16] D. Weller, A. Moser, L. Folks, M. E. Best, W. Lee, M. F. Toney, M. Schwickert, J.-U. Thiele, and M. F. Doerner, High K_u materials approach to 100 Gbits/in^2, IEEE Trans. Magn. **36,** 10 (2000).

[17] S. Iihama, A. Sakuma, H. Naganuma, M. Oogane, T. Miyazaki, S. Mizukami, and Y. Ando, Low precessional damping observed for $L1_0$-ordered FePd epitaxial thin films with large perpendicular magnetic anisotropy, Appl. Phys. Lett. **105,** 142403 (2014).

[18] T. Qu and R. H. Victora, Effect of substitutional defects on Kambersky damping in $L1_0$ magnetic materials, Appl. Phys. Lett. **106,** 072404 (2015).

[19] S. Iihama, A. Sakuma, H. Naganuma, M. Oogane, S. Mizukami, and Y. Ando, Influence of $L1_0$ order parameter on Gilbert damping constants for FePd thin films investigated by means of time-resolved magneto-optical Kerr effect, Phys. Rev. B **94,** 174425 (2016).

[20] S. Iihama, M. Khan, H. Naganuma, M. Oogane, T. Miyazaki, S. Mizukami, and Y. Ando, Magnetization dynamics and damping for $L1_0$-FePd thin films with perpendicular magnetic anisotropy, J. Magn. Soc. Jpn. **39,** 57 (2015).

[21] Z. Diao, Z. Li, S. Wang, Y. Ding, A. Panchula, E. Chen, L.-C. Wang, and Y. Huai, Spin-transfer torque switching in

magnetic tunnel junctions and spin-transfer torque random access memory, J. Phys. Condens. Matter **19**, 165209 (2007).

[22] C. Y. You, Effect of the synthetic antiferromagnetic polarizer layer rigidness on the spin transfer torque switching current density, Appl. Phys. Lett. **103**, 042402 (2013).

[23] X. G. Xu, D. L. Zhang, X. Q. Li, J. Bao, Y. Jiang, and M. B. A. Jalil, Synthetic antiferromagnet with Heusler alloy ferromagnetic layers, J. Appl. Phys. **106**, 123902 (2009).

[24] A. Bergman, B. Skubic, J. Hellsvik, L. Nordström, A. Delin, and O. Eriksson, Ultrafast switching in a synthetic antiferromagnetic magnetic random-access memory device, Phys. Rev. B **83**, 224429 (2011).

[25] K. Y. Camsari, A. Z. Pervaiz, R. Faria, E. E. Marinero, and S. Datta, Ultrafast spin-transfer-torque switching of synthetic ferrimagnets, IEEE Magn. Lett. **7**, 1 (2016).

[26] S. H. Yang, K. S. Ryu, and S. Parkin, Domain-wall velocities of up to 750 m/s driven by exchange-coupling torque in synthetic antiferromagnets, Nat. Nanotechnol. **10**, 221 (2015).

[27] S. Lepadatu, H. Saarikoski, R. Beacham, M. J. Benitez, T. A. Moore, G. Burnell, S. Sugimoto, D. Yesudas, M. C. Wheeler, J. Miguel, S. S. Dhesi, D. McGrouther, S. McVitie, G. Tatara, and C. H. Marrows, Synthetic ferrimagnet nanowires with very low critical current density for coupled domain wall motion, Sci. Rep. **7**, 1640 (2017).

[28] Y.-J. Chang, A. Canizo-Cabrera, V. Garcia-Vazquez, Y.-H. Chang, and T. Wu, Perpendicular magnetic tunnel junctions with synthetic antiferromagnetic pinned layers based on [Co/Pd] multilayers, J. Appl. Phys. **113**, 17B909 (2013).

[29] J.-B. Lee, G.-G. An, S.-M. Yang, H.-S. Park, W.-S. Chung, and J.-P. Hong, Thermally robust perpendicular Co/Pd-based synthetic antiferromagnetic coupling enabled by a W capping or buffer layer, Sci. Rep. **6**, 21324 (2016).

[30] S. Bandiera, R. C. Sousa, Y. Dahmane, C. Ducruet, C. Portemont, V. Baltz, S. Auffret, I. L. Prejbeanu, and B. Dieny, Comparison of synthetic antiferromagnets and hard ferromagnets as reference layer in magnetic tunnel junctions with perpendicular magnetic anisotropy, IEEE Magn. Lett. **1**, 3000204 (2010).

[31] A. Vaysset, C. Papusoi, L. D. Buda-Prejbeanu, S. Bandiera, M. Marins de Castro, Y. Dahmane, J.-C. Toussaint, U. Ebels, S. Auffret, R. Sousa, L. Vila, and B. Dieny, Improved coherence of ultrafast spin-transfer-driven precessional switching with synthetic antiferromagnet perpendicular polarizer, Appl. Phys. Lett. **98**, 242511 (2011).

[32] See Supplemental Material at http://link.aps.org/supplemental/10.1103/PhysRevApplied.9.044028 for the relative details on the information of a single-layer Fe-Pd thin film, the Fe-Pd PSAFM bottom free layer and [Co/Pd]$_n$ top reference layer, and $L1_0$ Fe-Pd SAFM PMTJ stack.

[33] D. A. Gilbert, L.-W. Wang, T. J. Klemmer, J.-U. Thiele, C.-H. Lai, and K. Liu, Tuning magnetic anisotropy in (001) oriented $(Fe_{1-x}Cu_x)_{55}Pt_{45}$ films, Appl. Phys. Lett. **102**, 132406 (2013).

[34] P. J. H. Bloemen, H. W. van Kesteren, H. J. M. Swagten, and W. J. M. de Jonge, Oscillatory interlayer exchange coupling in Co/Ru multilayers and bilayers, Phys. Rev. B **50**, 13505 (1994).

[35] S. S. P. Parkin, N. More, and K. P. Roche, Oscillations in Exchange Coupling and Magnetoresistance in Metallic Superlattice Structures: Co/Ru, Co/Cr, and Fe/Cr, Phys. Rev. Lett. **64**, 2304 (1990).

[36] S. Watanabe, T. Komine, T. Kai, and K. Shiiki, First-principle band calculation of ruthenium for various phases, J. Magn. Magn. Mater. **220**, 277 (2000).

[37] M. T. Rahman, A. Lyle, G. Hu, W. J. Gallagher, and J.-P. Wang, High temperature annealing stability of magnetic properties in MgO-based perpendicular magnetic tunnel junction stacks with CoFeB polarizing layer, J. Appl. Phys. **109**, 07C709 (2011).

[38] D.-L. Zhang, K. B. Schliep, R. J. Wu, P. Quarterman, D. Reifsnyder Hickey, Y. Lv, X. Chao, H. Li, J.-Y. Chen, Z. Zhao, M. Jamali, K. A. Mkhoyan, and J.-P. Wang, Enhancement of tunneling magnetoresistance by inserting a diffusion barrier in $L1_0$-FePd perpendicular magnetic tunnel junctions, Appl. Phys. Lett. **112**, 152401 (2018).

[39] C.-W. Cheng, T.-I. Cheng, C. H. Shiue, C.-L. Weng, Y.-C. Tsai, and G. Chern, Synthetic antiferromagnetic MgO/CoFeB/Ta(x)/CoFeB/MgO structures with perpendicular magnetic anisotropy, IEEE Trans. Magn. **49**, 4433 (2013).

[40] Y. Lu, M. Tran, H. Jaffrès, P. Seneor, C. Deranlot, F. Petroff, J.-M. George, B. Lépine, S. Ababou, and G. Jézéquel, Spin-Polarized Inelastic Tunneling through Insulating Barriers, Phys. Rev. Lett. **102**, 176801 (2009).

[41] Q. L. Ma, T. Kubota, S. Mizukami, X. M. Zhang, H. Naganuma, M. Oogane, Y. Ando, and T. Miyazaki, Interface tailoring effect on magnetic properties and their utilization in MnGa-based perpendicular magnetic tunnel junctions, Phys. Rev. B **87**, 184426 (2013).

[42] S. Yuasa and D. D. Djayaprawira, Giant tunnel magnetoresistance in magnetic tunnel junctions with a crystalline MgO (001) barrier, J. Phys. D **40**, R337 (2007).

[43] H.-R. Lee, K. Lee, J. Cho, Y.-H. Choi, C.-Y. You, M.-H. Jung, F. Bonell, Y. Shiota, S. Miwa, and Y. Suzuki, Spin-orbit torque in a bulk perpendicular magnetic anisotropy Pd/FePd/MgO system, Sci. Rep. **4**, 6548 (2014).

[44] H. A. Dürr, E. Dudzik, S. S. Dhesi, J. B. Goedkoop, G. van der Laan, M. Belakhovsky, C. Mocuta, A. Marty, and Y. Samson, Chiral magnetic domain structures in ultrathin FePd films, Science **284**, 2166 (1999).

[45] R. A. Duine, K.-J. Lee, S. S. P. Parkin, and M. D. Stiles, Synthetic antiferromagnetic spintronics, Nat. Phys. **14**, 217 (2018).